Final Draft

of the original manuscript

Liu, W.; He, W.; Jiang, H.; Wang, Q.; Chen, L.; Yang, Z.; Lin, Y.:

Influence of Graphene on Microstructure and Corrosion and Wear Resistance of Micro-Arc Oxidation Coatings on D16T Al Alloy Drill Pipe.

In: Journal of Materials Engineering and Performance. Vol. 30 (2021) 4162 - 4173.

First published online by Springer: 09.04.2021

https://dx.doi.org/10.1007/s11665-021-05727-y

Influence of Graphene on Microstructure and Corrosion and Wear Resistance of Micro-Arc Oxidation Coatings on D16T Al Alloy Drill Pipe

Wanying Liu, Wanying He, Hengyi Jiang, Qi Wang, Long Chen, Zhong Yang, and Yuxia Lin

Coatings were prepared on D16T Al alloy in electrolytes with and without graphene by micro-arc oxidation technology. Influences of graphene on the microstructure, corrosion and wear resistance of the coating were investigated. X-ray diffraction analysis result indicates that the coating is mainly composed of a-Al_2O_3, c-Al_2O_3 and Al substrate. c-Al_2O_3 was the dominant phase. The microstructure of coatings characterized by scanning electron microscopy, energy-dispersive x-ray spectroscopy and transmission electron microscopy shows the coating with graphene is flatter, denser, less pores and cracks than that of the coating without graphene. Moreover, the coating is consistent of a loose outer layer and dense inner layer. A little molten particles and many agglomerates accumulated on the surface of the coating. Graphene successfully embedded into the coating remarkedly decreased micro-pores and micro-cracks and slightly increased the thickness. The coating with graphene shows the better corrosion and wear resistance than the coating without graphene. The current potential, corrosion current density, wear and friction coefficient of coatings with graphene were 2 0.41 V, 3.97E28 A/cm^2, 1.57 mg and 0.68, respectively, revealing the desirable corrosion and wear resistance. The presence of graphene in coatings improved the thickness and microstructure and increased the corrosion and wear resistance of the coating.

Wanying Liu, School of New Energy and Materials (Southwest Petroleum University), Chengdu 610500 Sichuan, China; School of Materials Science and Engineering (Sichuan University), Chengdu 610065 Sichuan, China; and Institute of Materials Research, Helmholtz-Zentrum Geesthacht, Max-Plank-Str. 1, 21502 Geesthacht, Germany; and Wanying He, Hengyi Jiang, Qi Wang, Long Chen, Zhong Yang, and Yuxia Lin, School of New Energy and Materials (Southwest Petroleum University), Chengdu 610500 Sichuan, China. Contact e-mail: liuwanyingxx@163.com

1. Introduction

D16T Al alloy belongs to the hard aluminum alloy of aluminum-copper-magnesium series. It is widely applied to the aerospace, machinery, automotive, petroleum and other fields due to its low density, high specific strength, simple forming processing and excellent resistance to acid and alkali (such as H_2S and CO_2) (Ref 1, 2). Based on these excellent properties of D16T Al alloy, at present, it is gradually used as oil well pipe material in the oil and gas fields (Ref 3, 4), especially as the drill pipe material. However, the low hardness and poor wear resistance of aluminum alloy seriously restrict its extensive applications in the petroleum field. More and more scholars adopted various surface treatment technologies to improve the shortcomings of its low hardness and poor wear resistance, so as to broaden its application scopes and fields. Among them, the surface modification technologies for the common alu-minum alloys are anodic oxidation, electroplating, chemical plating, arc spraying, laser surface modification and micro-arc oxidation technology, which can significantly improve the overall performances of aluminum alloy materials (Ref 5, 6).

Micro-arc oxidation (MAO), also known as plasma electrolytic oxidation, is a new technology that uses in situ high-temperature sintering in the micro-arc zone to directly generate ceramic layers on the surface of light metals such as Al, Mg, Ti and their alloys. The ceramic coating prepared on the metal surface by MAO technology is firmly bonded to the substrate, owning a dense structure, good abrasion resistance, corrosion resistance, high-temperature impact resistance and other properties (Ref 7-9). However, many discharge channels form on the coating due to the spark discharges in MAO process and eventually solidify into micro-pores, causing the coating surface to display the rough and porous structure. Therefore, composite coatings were prepared by adding the nano-particles (such as nano-SiO_2, TiO_2, carbon nanotubes, graphite and graphene) into the electrolytes for improving the density, hardness, corrosion and wear resistance of the coatings (Ref 10). Babaei et al. (Ref 11) investigated the effect of nano-particles on the properties of the coating formed on the aluminum alloy and found that these additives could decrease the penetration and rate of corrosive ions into coatings by contributing and absorbing these additives in plasma electrolytic oxidation (PEO) coatings, and as a result declining the number and size of cracks or pores and raising the thickness and density of coatings and so increase corrosion protection. Fatimah et al. (Ref 12) studied the effect of nano-ZrO_2 particles on the corrosion and wear resistance of MAO coatings on the surface of TC4 alloy. Results show that the main constituent phases of the coating are ZrO_2, $ZrTiO_4$, TiO_2, Ti_2O, Al_2O_3 and SiO_2. With the increase in nano-ZrO_2 concentration, the number and size of the micro-pores reduced. When the concentration of ZrO_2 is 9 g/L, the corrosion and wear

resistance of the coating are the best. Ma et al. (Ref 13) studied the effect of nano-SiO_2 on the growth rate and properties of MAO coating formed on the surface of aluminum alloys. Results show that the growth rate of MAO coating increased because an ''impurity discharge'' formed during the breakdown process of aluminum alloy after adding nano-SiO_2, narrowing the forbidden band width of the coating and promoted MAO electrical breakdown process to improve the growth rate of MAO coatings. In recent years, the reports that the properties of MAO coating can be improved by adding graphene and graphene oxide to the electrolyte occurred (Ref 14, 15). Liu (Ref 16) prepared MAO coating on TC4 titanium alloy drill pipe by adding graphene to improve the wear and corrosion resistance of the titanium alloy drill pipe. Khakzad et al. (Ref 17) studied the effect of alumina-silica on the microstructure, phase and corrosion behavior of the composite coatings prepared on aluminum by plasma electrolytic oxidation and revealed that the alumina-silica composite coating considerably improved the corrosion resistance of the aluminum. Ma et al. (Ref 18) uniformly dispersed the carbon material into the electrolyte by mechanical stirring and ultrasonic action and formed the carbon-containing coating with a dense structure and excellent abrasion resistance. Chen et al. (Ref 14) fabricated MAO ceramic coating with graphene on the surface of aluminum alloy by dispersing graphene into the electrolyte. Results showed that the breakdown voltage of the coating decreased due to the addition of graphene and promoted the growth of the coating. Lv et al. (Ref 19) prepared graphite-coated coating with dense structure and good corrosion resistance by adding graphite to the electrolyte. The macro-effect of additives on the properties of the coating was discussed in these studies. Liu et al. (Ref 5) studied the influence mechanism of graphene on the micro-area electro-chemical corrosion of the coated aluminum alloy. However, less research on effect of additive particles (especially graphene additive) on the discharge channels during the formation process of the coating, and few studies on the effect of different coating morphologies on the properties of the coating are reported. In the present work, the influence of graphene on the formation of MAO coating on D16T Al alloy was studied and discussed, and then the effect mechanism of incorporated graphene on the microstructure, wear and corrosion resistance of the coating was investigated, which provided a theoretical basis for the application of micro-arc oxidation technology on the surface treatment of aluminum alloy as the drill pipe used in the oil and gas field.

2. Experimental Procedures

D16T Al alloy used as the oil well drill pipe material was provided by Tarim oilfield, China. The prepared specimens with the dimension of 15 mm 9 15 mm 9 5 mm were grounded using abrasive paper until #1200 grit and ultrason-ically cleaned in acetone. Its chemical composition (mass fraction) is 3.85% Cu, 1.29% Mg, 0.65% Mn, 0.068% Si, 0.11% Fe, 0.049% Ti, 0.054% Zn and balance Ti. Lamellar graphene was used as the additive. The SEM morphology of graphene is shown in Fig. 1. The added graphene concentration is 2 g/L. The PEO process is carried out using a constant current MAO device of WDL20-6, consisting of a micro-arc oxidation power source, a stainless steel cathode, an oxidation

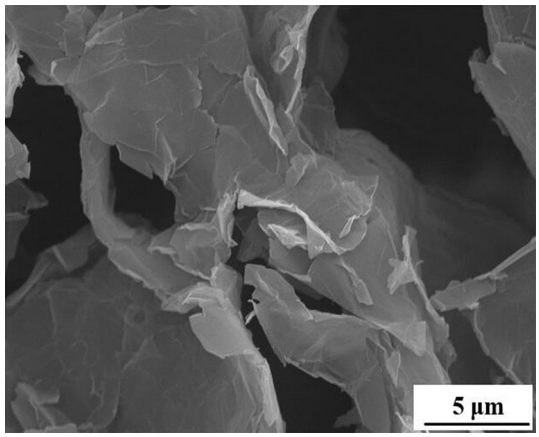

Fig. 1 SEM image showing the morphology of graphene additive

electrolytic cell, a stirring system and a cooling system which maintained the electrolyte temperature below 298 K to stabilize the electrochemical reaction accompanying plasma discharges. The electrolyte consisted of 11.65 g/L Na_2SiO_3, 1.42 g/L NaOH, 2 mL/L $C_3H_8O_3$ and 6 g/L $Na_6O_{18}P_6$. The MAO coatings with and without graphene are denoted as G2 and G0, respectively. The graphene suspension with the strong hydrophobicity was uniformly distributed in the electrolyte by magnetic stirring. The pH value of the electrolytes with and without graphene was tested by a Metrohm 691 pH meter, and they were 13.20, 13.16, respectively. In MAO treatment process, a current density of 4 A/dm^2, a frequency of 150 Hz, a duty cycle of 20% and the oxidation time of 10 min were set. The constituent phases of the coatings were tested by x-ray diffraction (XRD, DMAX-3A) (Cu Ka radiation, the wavelength k = 1.5406 Å) with a step size of 0.02 and a scan range from 10° to 80°. Scanning electron microscope (SEM, TESCAN Vega 3 SB) was used to inspect the surface and cross-sectional microstructure of the coatings. The elemental com-position of the coatings was analyzed by an energy-dispersive x-ray spectroscope (EDS) detector in conjunction with the mentioned SEM. For further evaluating microstructure and verifying graphene additive successfully incorporated to the coating G2, transmission electron microscope (TEM, JEL-2100) was used to investigate the cross-sectional microstructure of G2. The roughness of MAO coatings and substrate was measured by the roughness tester (TR200). Their micro-hardness was tested by micro-Vickers hardness tester (HV-1000) with the load of 100 g and the holding pressure time of 20 s. The multifunctional material surface tester (MFT-4000) was used to test the wear loss and friction coefficient of the coatings and substrate under the dry experiment conditions at room temperature. A steel ball with a radius of 6 mm was used for grinding. The wear time was 2400 s with a load of 5 N, and the sliding speed was 5 mm/s. The corrosion behavior of the coatings and substrate immersed in 3.5 wt.% NaCl solution for 2 h was investigated through the electrochemical impedance spectroscopy (EIS) and potentiodynamic polarization (Tafel) curve measurements by the scanning electrochemical micro-scope (CHI900C). A saturated calomel electrode (SCE) was used as the reference electrode. The platinum plate was used as the counter electrode. D16T Al alloy and its coatings were used as the working electrode. The exposed area of the samples was 1 cm^2. EIS was performed between 0.01 Hz and 100 kHz

frequency, and the obtained EIS experimental data were simulated and analyzed by ZsimpWin software. Potentiodynamic polarization tests were carried out from 0.5 V to + 1.0 V vs. OCP at a scanning speed of 1 mV/s. The values of corrosion potential (E_{corr}), corrosion current density (i_{corr}), corrosion rate as well as other parameters were determined by the analysis result of potentiodynamic polarization curves.

3. Results and Discussion

3.1 Phase Analysis of the Coatings

XRD patterns of D16T Al alloy drill pipe substrate, the coated samples G0 and G2 are shown in Fig. 2. It is clearly found that the coatings mainly consisted of Al matrix, a-Al_2O_3 and c-Al_2O_3. The content of c-Al_2O_3 in the coating G2 is the most, and its diffraction peak intensity is the largest. The obvious amorphous phase (corresponding to the ''small hill'' at 15° ~ 30° in XRD spectrum of 2h) and a high aluminum diffraction peak are found in G0. Aluminum diffraction peaks appeared because x-rays could pass through the micro-pores and the thin dense inner layer of the coating and hit the substrate, so the strong diffraction peak of Al matrix was obtained. Compared to G0, the diffraction peaks of a-Al_2O_3 and c-Al_2O_3 of G2 increased greatly, but the peak value of aluminum diffraction peaks decreased significantly. The phase a-Al_2O_3 with high melting point, high hardness, wear resistance, acid and alkali resistance is the most stable phase of alumina. The phase c-Al_2O_3 is a transitional metastable phase that undergoes an irreversible phase transition around 1200 °C, and it is transformed to a-Al_2O_3. Alumina tends to solidify and forms c phase at a fast cooling rate and then tends to form a phase at a relatively low cooling rate (Ref 20).

In MAO process, because the molten matrix and oxide were produced from the arc discharge, ejecting from the discharge channel and flowing along the surroundings and then quenching occurred when the electrolyte cooled quickly, the unstable c-Al_2O_3 formed on the outer layer of the coating. c-Al_2O_3 heat-shielding layers covered the inner layer and increased the temperature of the inner layer. The melt cooled down slowly when the inner layer temperature was enough high. Finally, the unstable c-Al_2O_3 transformed to the stable a-Al_2O_3 (Ref 21, 22). According to the literature (Ref 23-25), the conductivity and melting point of the coating components formed at the anode/electrolyte interface are two important factors that significantly affect the voltage of the electrolyte. The voltage is affected by the melting point of the oxide component at the anode/electrolyte interface. The components with higher melting have higher voltages. The higher the voltage is, the more intense the spark discharge is. That causes the electrolyte to have higher reaction temperature compared to the electrolyte with weaker spark discharge. Therefore, more c-Al_2O_3 converted into a-Al_2O_3.

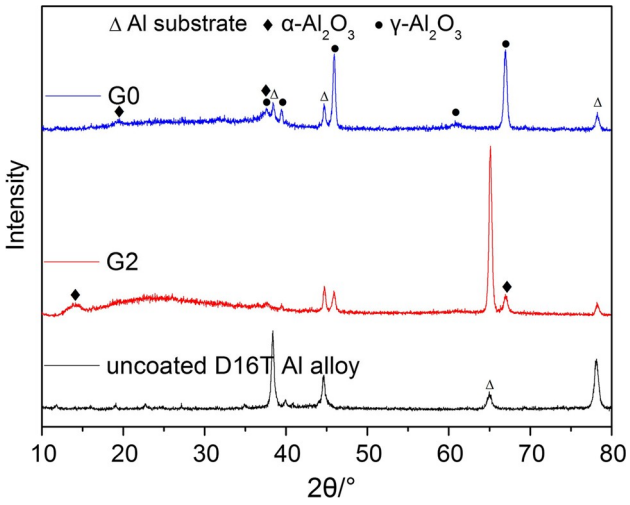

Fig. 2 XRD patterns of G0, G2 and the uncoated D16T Al alloy

3.2 Morphology and Composition of the Coatings

Figure 3 and 4 are SEM images of MAO coatings G0 and G2 morphologies, respectively. From Fig. 3, it can be seen that the surface of the coating G0 with many micro-cracks is rough, and a large number of rapidly solidified rough molten particles, lumps and the flowing traces. No flat structure can be observed at the magnification image of 20009, and the micro-pores on the surface of the coating were small and numerous. Figure 4 shows that the surface of the coating G2 with fewer molten particles is flat. A clear planar structure can be observed at the magnification image of 20009. Compared to G0, the number of the micro-pores on G2 surface is fewer, but the size became larger. It can be seen that graphene filled and covered the pores (shown by the white dotted line frame in Fig. 4b), and the micro-cracks on the surface of the coating are fewer. For furtherly judging the substance in the white dotted line frame in Fig. 4(b) is graphene, EDS tests were performed on regions 1 and 2 in Fig. 4(b). The results are shown in Fig. 5(a) and (b). Main components of the coating are C, Al, O, Si, Na, Au and a small amount of P. Au is from sprayed Au on the coating for preventing the coating from being electrically charged due to the non-conductivity, and C is from graphene. Al is from the alumina ceramic coating produced by the reaction product of the substrate with the anionic substance in the electrolyte. O, Si, Na and P are all compounds containing O, Si, Na and P produced by the reaction of the substances in the electrolyte. The tested results from Fig. 5 are compared and analyzed. It can be known that C content in region 2 is significantly higher than that in region 1, indicating that the substance shown by the white dotted line frame in Fig. 4(b) is graphene which keeps its original state. In summary, EDS test results show that graphene successfully incorporated to the prepared coating during MAO process and filled the pores in the coating.

Figure 6 is the cross-sectional morphologies of G0 and G2. From Fig. 6, it can be obviously found that the coating of G0 and G2 is composed of the outer loose layer and inner dense layer, agreeing with the research findings (Ref 26). The coating G0 displays the uneven surface with many pores and micro-cracks (illustrated in Fig. 6a). The thickness of the coating is 26 **1**m, and the inner layer thickness is 0.6 **1**m. The surface of G2 is flat, dense and a few pores. The thickness of the whole coating is 30 **1**m, and the thickness of the inner dense layer is 1 **1**m. In MAO process, the voltage is the driving force. The larger the voltage is, the stronger the electric field strength in the electrolyte is. That promotes the formation process of the coating and thicker coating can be obtained. The size and energy of the spark obviously increased with the coating thickness. That makes the molten pool on the surface erupt violently, and the molten pool's size increases (Ref 27). The

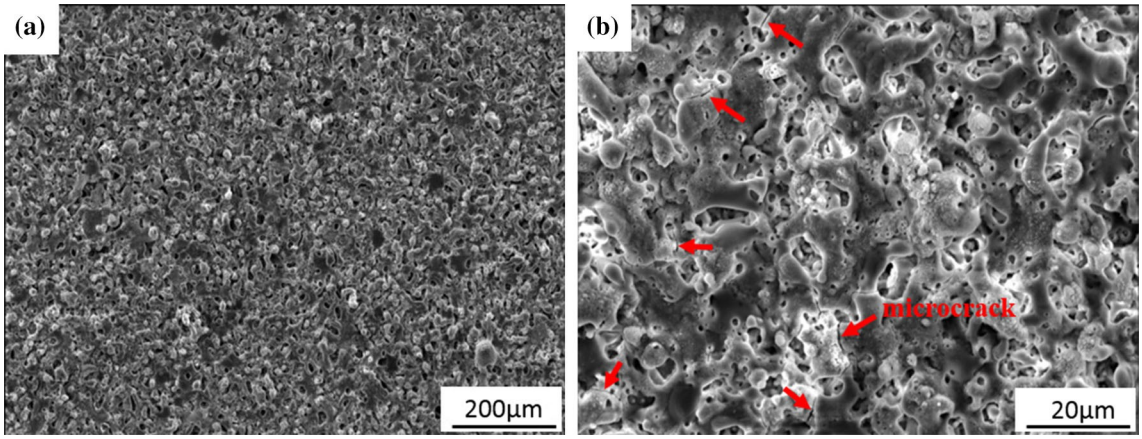

Fig. 3 SEM micrographs of surface of the coating G0: (a) 2009; (b) 20009

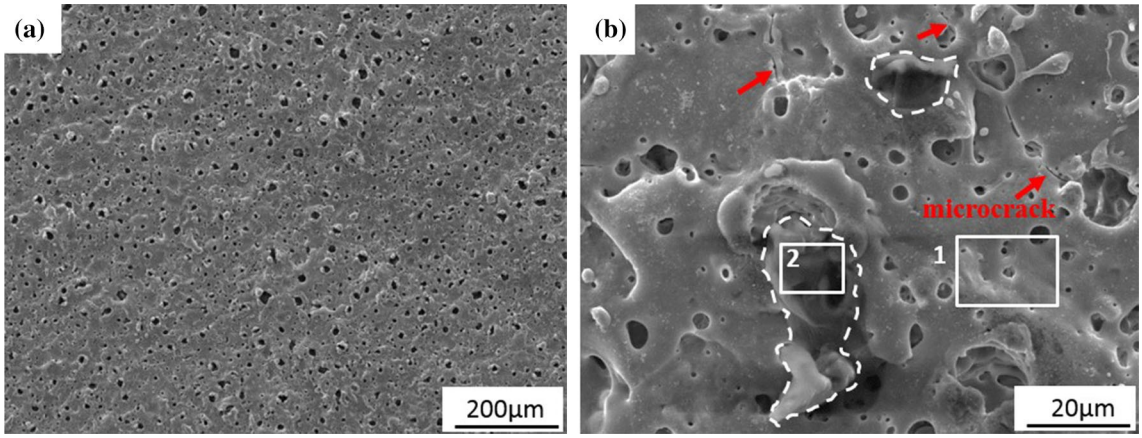

Fig. 4 SEM micrographs of surface of the coating G2: (a) 2009; (b) 20009

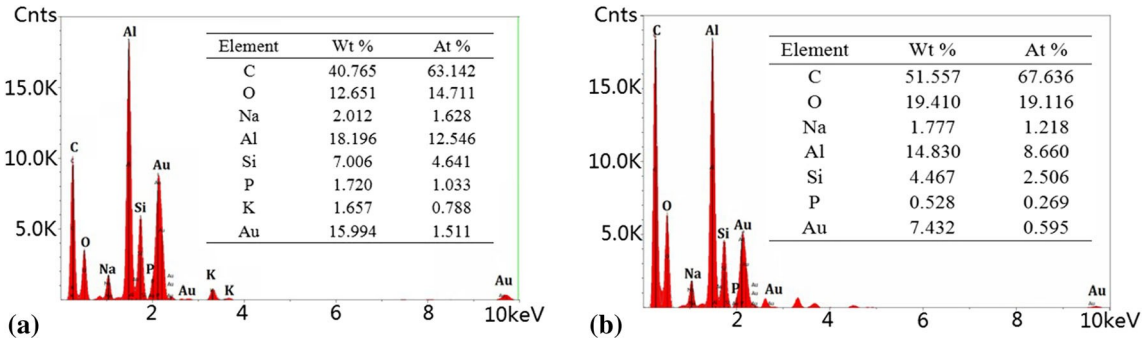

Fig. 5 EDS patterns of the area 1 and 2 of the coating G2 in Fig. 4(b): (a) area 1 and (b) area 2

electrons of graphene can move freely and own super-conductivity (10^6 S/m) and good heat transfer (3000 W/m K) due to graphene with two-dimensional sheet structure when C atom *sp*2 is hybridized to form large p bonds in the carbon ring (Ref 28). So the pores' size on the surface of the coating gets bigger and the thickness of the coating increases.

Figure 7 is TEM images of the cross section of the coating G2. It is clearly seen that the coating has an inner layer and a porous outer layer, which is consistent with Fig. 6. Obviously, the right part of Fig. 7(a) shows TEM image of D16T Al alloy substrate. The left part of Fig. 7(a) shows TEM image of the microstructure of the coating containing inner layer and outer layer. Within the inner layer, the coating has a non-porous layer. The thickness is about 1 **1**m. Graphene embedded in the porous outer layer can be obviously observed in Fig. 7(a) (shown in the red dotted line area). Its magnified image is displayed in Fig. 7(b). Clear graphene morphology can be seen. It was furtherly confirmed that graphene successfully incorporated in the coating through TEM diffraction pattern image of the white rectangle area (Fig. 7c) and the high-resolution transmission electron microscopy (HRTEM) of the white rectangle area in Fig. 7(c) (indicated in Fig. 7d).

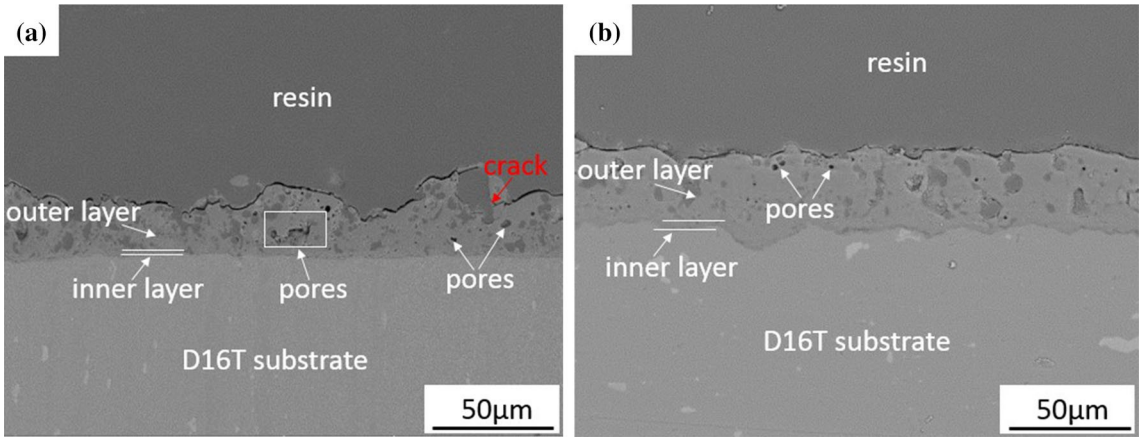

Fig. 6 SEM-BSE micrographs of cross section of the coatings G0 and G2: (a) G0, (b) G2

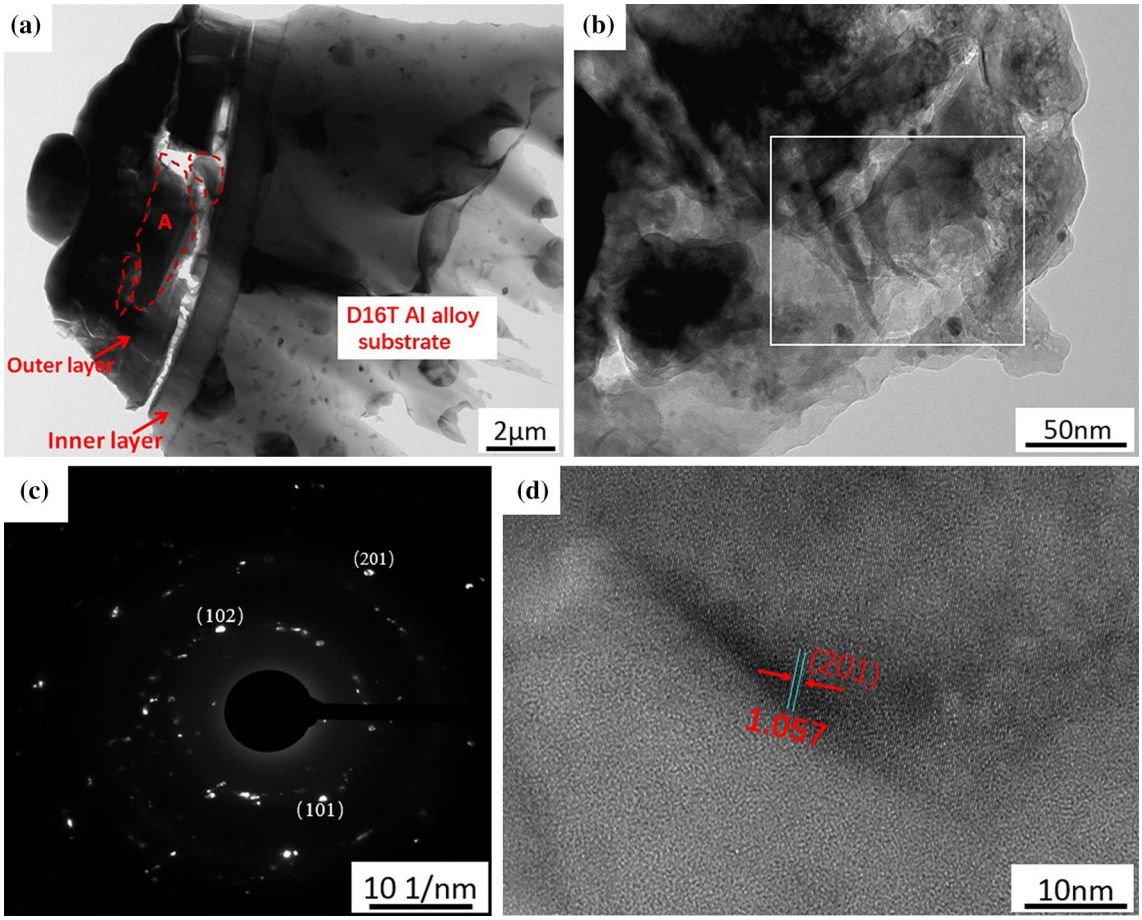

Fig. 7 (a) TEM bright-field image of the cross-sectional micrographs of G2, (b) TEM bright-field image of the area A, (c) selected area diffraction patterns taken from the white rectangle area and (d) HRTEM image of the white rectangle area

Figure 8 is SEM map images of the element distribution of the coating G2. It can be known that most surface areas of the coating contain Al and O elements. According to the study on the discharge mode during MAO process by Hussein (Ref 29) and Cheng (Ref 30), and combining with the analysis results in Fig. 8, the conclusion that a large amount of alumina formed after the condensation of the squirting molten material between the oxide layer and the substrate on the surface can be obtained. Si and Na participate in the formation of coating. Si mainly distributes on the smooth and the protruding area of the surface, which participates in the coating formation by the bubble breakdown discharge during the reaction. Na distributes in the micro-pores and the content of Al in some micro-pores is extremely low. It is caused by the discharge which is ascribed to the bubbles in the outer layer or the bubbles contacting to the surface of the coating. Higher aluminum content formed on the part of surface due to the bubble breakdown discharge. The C element mainly distributes on the coating surface in two types.

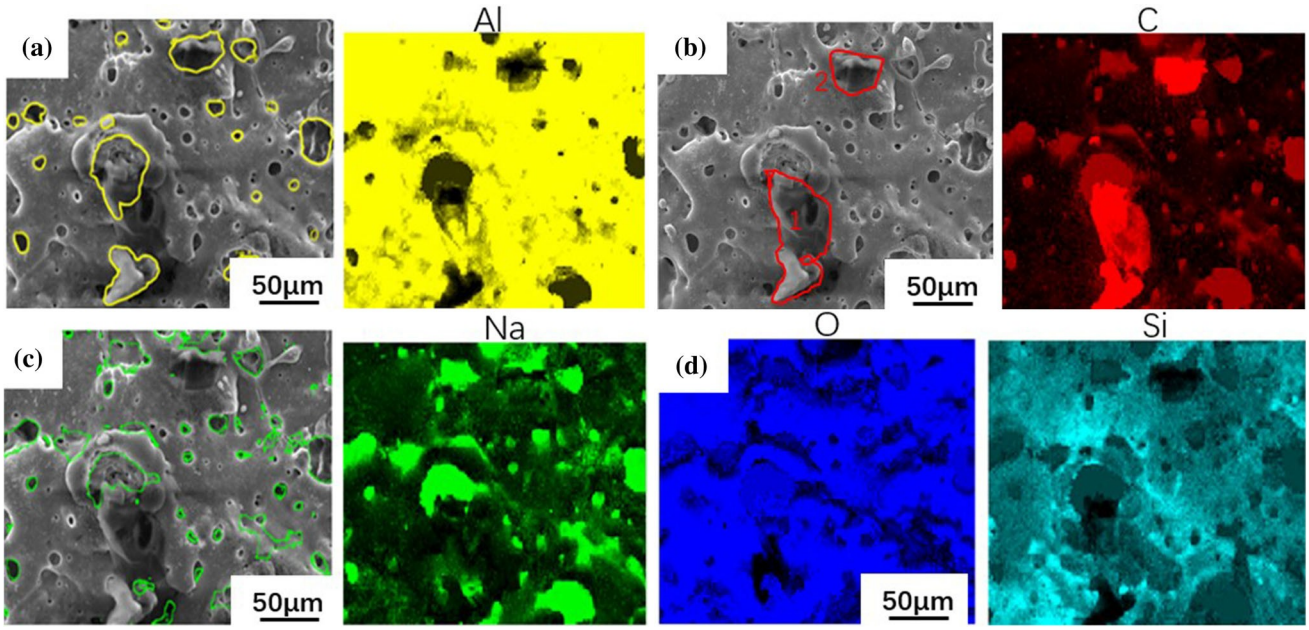

Fig. 8 Cross-sectional elemental map of G2: (a) Al; (b) C; (c) Na; and (d) O, Si

The first type basically coincides with the distribution of Na. Graphene participates in the coating formation by bubble breakdown discharge, entering the micro-pores with the electrolyte. The second type is shown in regions 1 and 2 in Fig. 8(b). Graphene on the surface of these regions forms clumps, and the content of C and O is higher than that of other regions. Here, graphene exists in its original state, so C distribution in bright colors can be clearly seen, and the C element from other regions is darker except for regions 1 and 2. Graphene in these regions occurred chemical reactions after melting and existed as a compound (Ref 31). Since graphene existed as a layer of nanosheets, it is prone to agglomeration due to the strong van der Waals bond. Parts of graphene in the electrolyte are adsorbed on the surface of the coating during MAO process. When pores are around it, and oxide film melts because the breakdown discharge occurs. Graphene mixes with the solid and liquid of the melt, and it is condensed with the electrolyte after the heat exchange. The solidified melt has a bonding effect on graphene, so graphene forms rough protrusions on the surface of the coating. Combining with the analysis of the coating phase and the morphological characteristics, the discharge process during the formation of the coating with graphene during MAO process can be divided into A, B, C and D types (shown in Fig. 9). Discharge of type A is caused by the breaking down of bubbles in the outer layer or bubbles contacting with the surface of the coating. That causes elements to deposit in the electrolyte, and the rough protrusions form on the surface of the coating by the discharge product combining with the molten coating product form. Discharge of type B is a breakdown discharge at the interface between the film layer and the substrate, which causes the molten alumina in the inner layer to be ejected from the molten pool and flow to the surroundings. The flow traces around the micro-pores form when the electrolyte quenched. Discharge of type C is the breakdown discharge of bubbles of the pores and cracks in deeper area under the surface of the coating, and smooth protrusions form. Discharge of type D is the breakdown discharge in larger pores near the interface between the inner

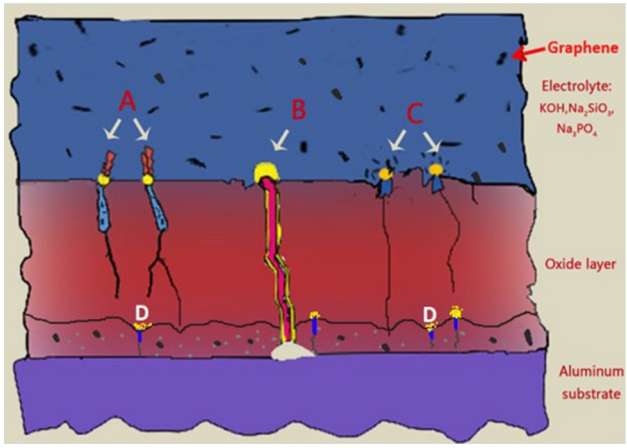

Fig. 9 Schematic diagram of the discharge model of MAO process for aluminum alloy in electrolyte with graphene

layer and outer layer of the coating, causing the coating to grow inward and promoting the element absorption in the electrolyte. The coating with various surface formed by different discharge types has different morphology characteristics and elemental distribution.

3.3 Roughness and Micro-Hardness of the Coatings

Figure 10 shows the roughness and micro-hardness test results of the uncoated D16T Al alloy, G0 and G2. From Fig. 10(a), it can be seen that the roughness of the uncoated D16T Al alloyis 1.2 **1**m, and the roughness of G0 and G2 significantly increases to 3.8 and 2.2 **1**m, respectively. How-ever, the roughness of G2 reduced compared to that of G0. That is because the pores and micro-cracks formed in the discharge channels during MAO process was filled by graphene. The smaller-sized melt droplets generated in the process of MAO reaction will melt and spread with graphene and the coating. Subsequently, the smooth, flat and dense surface formed after

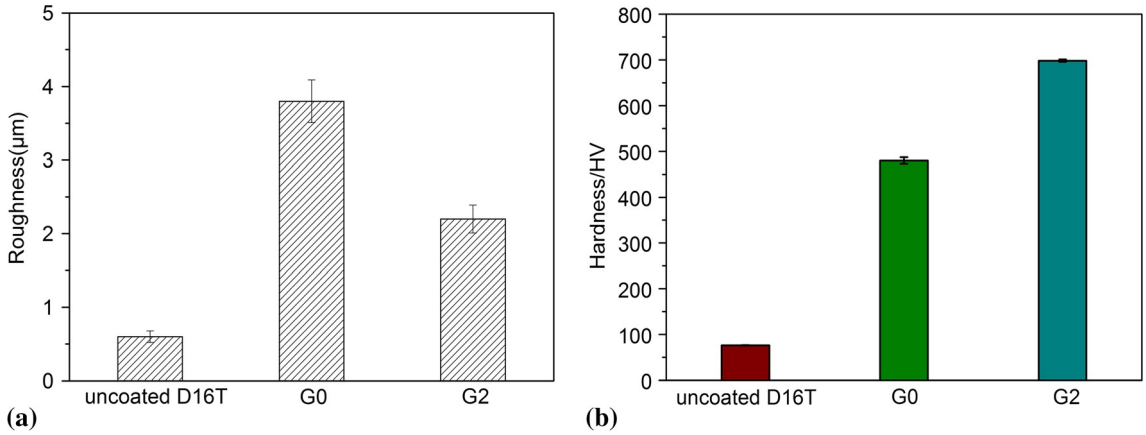

Fig. 10 Roughness (a) and micro-hardness (b) of the uncoated D16T Al alloy, G0 and G2

the melt droplets disappearing. However, the surface of G0 exhibits the uneven characterization because many pores and cracks are not filled by graphene, and the melts deposit at different stages. Therefore, the roughness of G0 is larger than that of G2.

The micro-hardness value of the uncoated D16T is greatly improved after MAO treatment (illustrated in Fig. 10b). The micro-hardness value of G0 is 4 times higher than that of the uncoated D16T. The micro-hardness of G2 is 7 times higher than that of its matrix, and it is about 2 times higher than that of G0, indicating that graphene significantly improved the micro-hardness of the coated aluminum alloy. Lee et al. (Ref 32) measured the Young's modulus and intrinsic strength of unsupported single-layer graphene oxide by nano-indentation. Results showed that the single-layer graphene oxide had an elastic modulus of 1 TPa. The distribution mode improved the anti-load capacity of the coating to a certain extent. Additionally, c-Al_2O_3 and a-Al_2O_3 phases form in the MAO process, so the micro-hardness of the coatings is much larger than that of the substrate. It is well known that Al_2O_3 has excellent properties of high strength and high hardness. Moreover, Al_2O_3 ceramic coating owns the excellent properties of wear resistance, corrosion resistance, high temperature and pressure resistance, high hardness, no aging and withstanding harsh environmental conditions for normal work. Therefore, c-Al_2O_3 and a-Al_2O_3 phases of the coating are important factors for improving the micro-hardness of the coating. R. Pérez-Bustamante et al. (Ref 33) studied the effect of graphene on the microstructure and hardness of Al. Results showed that graphene had a positive effect on the hardness, smaller roughness and higher hardness, which can improve the abrasion resistance of the coated samples.

3.4 Corrosion Resistance of the Coatings

Potentiodynamic polarization curves are shown in Fig. 11, and the correlative electrochemical parameters obtained from polarization curves are displayed in Table 1. According to formula (1) and Stem-Geary formulas (2) and (3) (Ref 33), polarization impedance (R_p) and corrosion rate can be calculated out.

$$R_p = \frac{b_a b_c}{2.303 i_{corr}(b_a + b_c)} \quad (Eq\ 1)$$

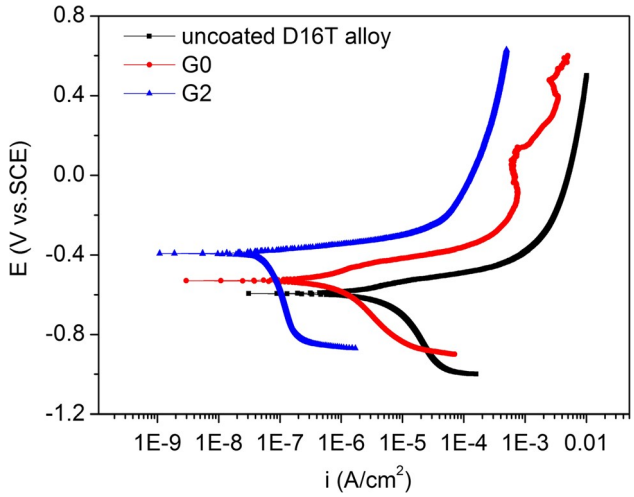

Fig. 11 Polarization curves of the uncoated D16T alloy, G0 and G2 in 3.5 wt.% NaCl solution

$$J_{corr} = k/R_p \quad (Eq\ 2)$$

$$k = b_a b_c/2.303(b_a + b_c) \quad (Eq\ 3)$$

From Table 1, it can be seen that the self-corrosion potential (E_{corr}), the self-corrosion current density (I_{corr}) and the corrosion rate of G0 are − 0.53 V, 3.15E− 7 A/cm^2 and 3.69E−3 mm/a, respectively, whereas G2 owns the E_{corr} of − 0.41 V and I_{corr} of 3.97E−8 A/cm^2, reducing an order of magnitude. The polarization resistance increased an order of magnitude, showing more visible passivation area. The fitted corrosion rate of G2 is 4.66E−4 mm/a. In summary, the corrosion resistance of the coated samples is greatly improved after MAO treatment, especially for G2 with excellent microstructure.

The obtained impedance data of the uncoated D16T Al alloy and the coated samples (G0, G2) are displayed in Fig. 12 in form of Nyquist plots and Bode plots. It can be seen that the coating has capacitive reactance arcs in the mid-high frequency region, and the capacitive reactance arc radius of G2 is larger than that of G0 from Fig. 12(a). The larger the capacitive resistance arc is, the better the corrosion resistance of the coating has. The ability providing corrosion protection for the

Table 1 Electrochemical polarization data of coated samples immersed in 3.5 wt.% NaCl solution

Sample	E_{corr} (V vs. SCE)	I_{corr}, A/cm^2	b_a, mV/dec	b_c, mV/dec	Corrosion rate, mm/a
G0	−0.53	3.15E−7	97.78	108.06	3.69E−3
G2	−0.41	3.97E−8	42.82	118.40	4.66E−4

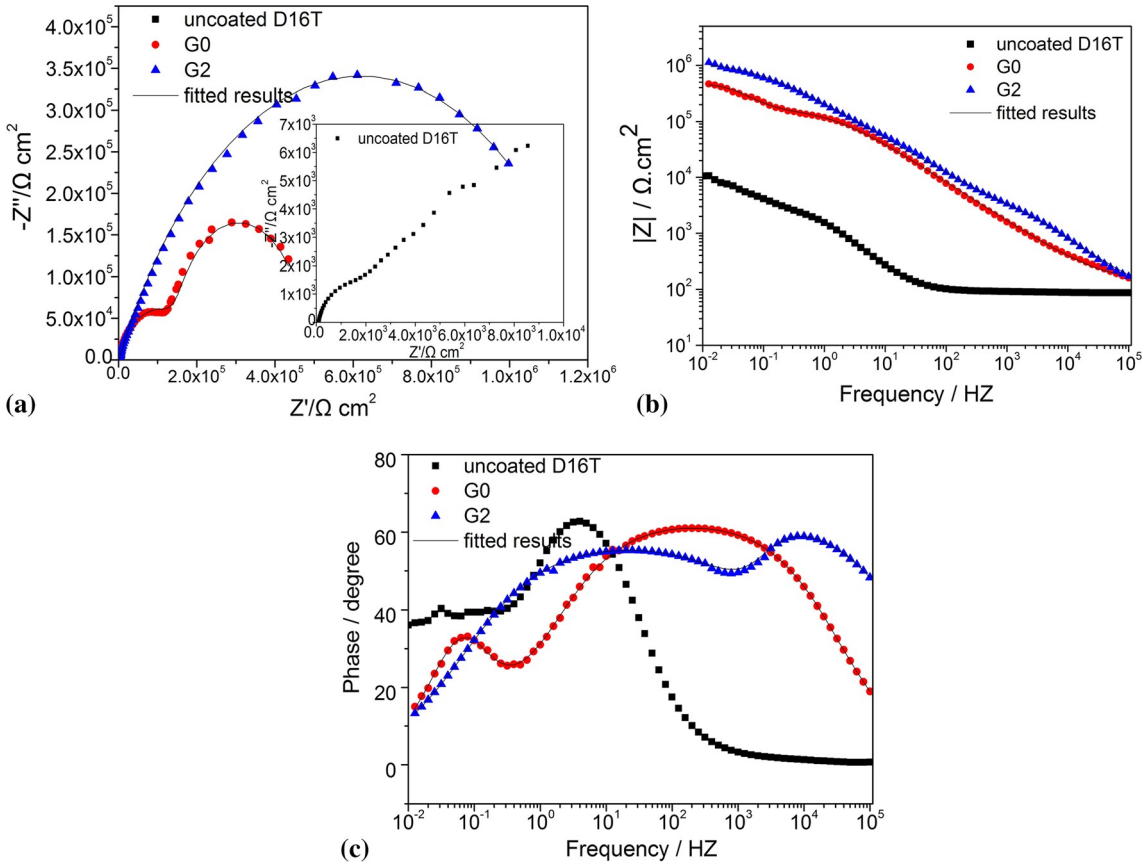

Fig. 12 EIS spectra of the uncoated D16T and coated samples immersed in 3.5 wt.% NaCl solution for 2 h: (a) Nyquist plots and (b, c) Bode plots

internal matrix material is greater. That is consistent with the kinetic potential polarization curve test results. In Fig. 12(b) and (c), if the impedance value in low-frequency region is higher, the coating will own better corrosion resistance. The impedance value of the substrate in low-frequency region is 10^4 X cm^2, and it increases to 10^5 X cm^2 after MAO treatment. In particular, the low-frequency impedance of G2 increases to 10^6 X cm^2 due to the graphene successfully incorporated into the coating and filled the pores and micro-cracks, so its corrosion resistance was significantly improved.

The Nyquist curve fitting circuit is shown in Fig. 13 (Ref 34, 35), and the fitted parameter results are displayed in Table 2. In the equivalent circuit, Rs is the solution resistance between the working electrode and the reference electrode. R1 is the external bulk layer resistance of coated samples. CPE1 is the constant phase element of the external bulk layer. R2 is the resistance of the inner dense layer, and CPE2 is a constant phase element representing the inner dense layer. The inner-layer impedance of the coating is much higher than that of the outer layer, indicating that the inner dense layer plays an

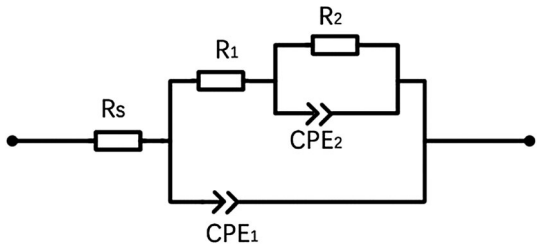

Fig. 13 Equivalent circuit of the coated samples in 3.5 wt.% NaCl solution

important role of the main corrosion resistance function. The resistance of the outer layer and inner layer of G2 is larger than that of G0. That is ascribed to graphene incorporated into the coating and filled the pores and prevented the invasion of corrosive ions. In addition, graphene inhibits the diffusion pathway of aggressive electrolyte and is often used as a good barrier against ion penetration (Ref 36). The protective coating

Table 2 Electrochemical parameters obtained from EIS spectra of G0 and G2

Sample	Rs, X cm^2	R1, X cm^2	CPE1		R2, X cm^2	CPE2	
			Y1, F	n1		Y2, F	n2
G0	135.90	1.57E5	1.24E−6	0.71	3.07E5	1.25E−5	0.83
G2	45.24	1.98E5	9.62E−8	0.59	1.24E6	1.35E−6	0.64

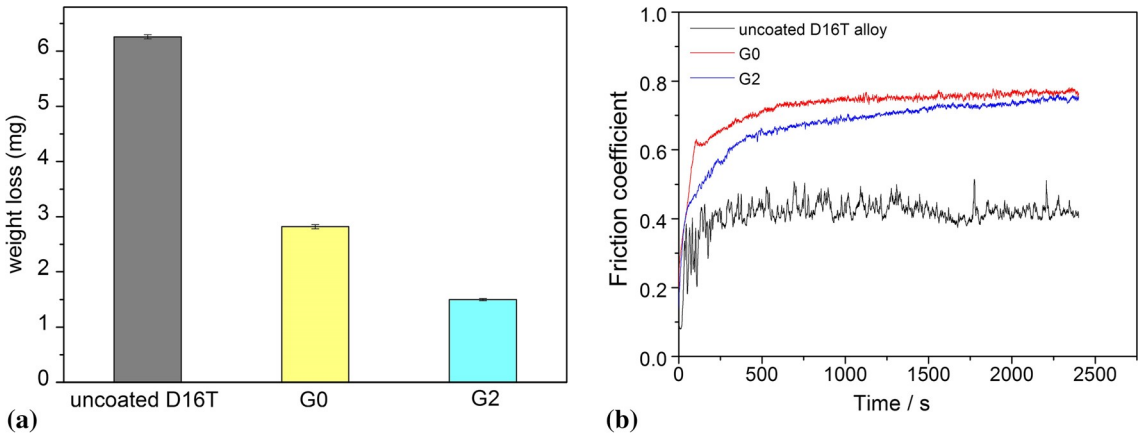

Fig. 14 Weight loss (a) and friction coefficient as a function of the time (b) of uncoated D16T, G0 and G2

graphene can be also used as inhibitor to prevent the underlying metal from being corroded when they work in a corrosive medium for a long time. Literature (Ref 20, 37) has confirmed that ultra-dense carbon atom network forming graphene is completely impermeable, preventing material from being corroded. Graphene promotes the materials to own the chemical stability. Furthermore, graphene is an electron-rich material that accelerates oxidation reactions and produces more corrosion-resistant oxides. Therefore, it has cathodic protection against corrosion.

3.5 Wear Resistance of the Coatings

The weight loss and friction coefficient of the uncoated D16T, G0 and G2 are shown in Fig. 14, and their wear track morphologies are displayed in Fig. 15. Figure 14(a) shows the wear loss of the uncoated D16T is the largest, which is 6.3 mg. The wear is the most serious. However, the wear loss of the coated samples sharply decreases, especially for G2. Its wear loss is 1/4 times than that of the substrate. Figure 14(b) shows the friction coefficient of the substrate is 0.4 and the fluctuation range is large. The width of the wear scar is 1108.33 **1**m. The obvious furrow marks distribute on the surface, indicating severe adhesive wear occurred. The friction coefficient of G0 is the largest. It is about 0.75 in the stable stage, and the width of the wear scar is 776.42 **1**m. Some small and grinding ceramic particles scattered on the surface of the wear scar, indicating that abrasive wear occurred. The friction coefficient of G2 reduces to 0.68 compared to that of G0, but the friction coefficient increased slightly with the increase in the wear time. The width of the unobvious wear scar is 648.17 **1**m. Some scattered small particles can be observed in the enlarged SEM images. The micro-pores are filled with scattered abrasive particles. It is well known that the wear resistance of D16T Al alloy is greatly improved after MAO treatment from Fig. 14(b), especially for the coating with graphene. The graphene with the perfect lamellar structure and low surface energy exhibits promising wear resistance. Additionally, the adhesion and wear resistance of the coating with graphene sheets can be improved by hydrogen-induced flexible electrons of graphene. The higher adhesion of graphene originates from hydrogen adsorption, and it is helpful to extend the wear life of the coating by hydrogen passivation from the graphene (Ref 38). Figure 15 shows that the wear mechanism between the substrate and the coated samples is different. After MAO treatment, the wear changes from the adhesive wear of the substrate to the abrasive wear of the coated samples. For further explaining the wear mechanism, the EDS analysis on the surface of the wear scar is performed and results are shown in Table 3. From Table 3, it can be seen that Al content of the substrate surface after wear is 81.185 and oxygen content is 12.435, indicating the substrate and the thin aluminum film layer formed by the surface oxidation were worn off. The surface of the substrate is smooth, but the hardness is low. Therefore, it shows very poor abrasion resistance. The aluminum-to-oxygen ratio on the surface of G0 is close to 1.85:1. The Fe content is 10.96 and the Gr content is 0.169, indicating that the coating is very thin after the wear and parts of the substrate are exposed. The friction pair GCr15 steel ball is also worn to a certain extent because the high hardness of Al_2O_3 (Ref 39) and the hard particles are worn off and easily penetrated to the pores and cut the coating. The surface of the friction pair meshes with each other, resulting in the friction coefficient increase. But the hardness of G0 is high and the wear resistance is still better than that of the substrate. The aluminum-to-oxygen ratio of G2 is close to 1:1. The Fe and Gr content increases more twice than that of G0. Furthermore, much more C appearance indicates the coating is still intact after wear compared to the substrate and G0, and its wear

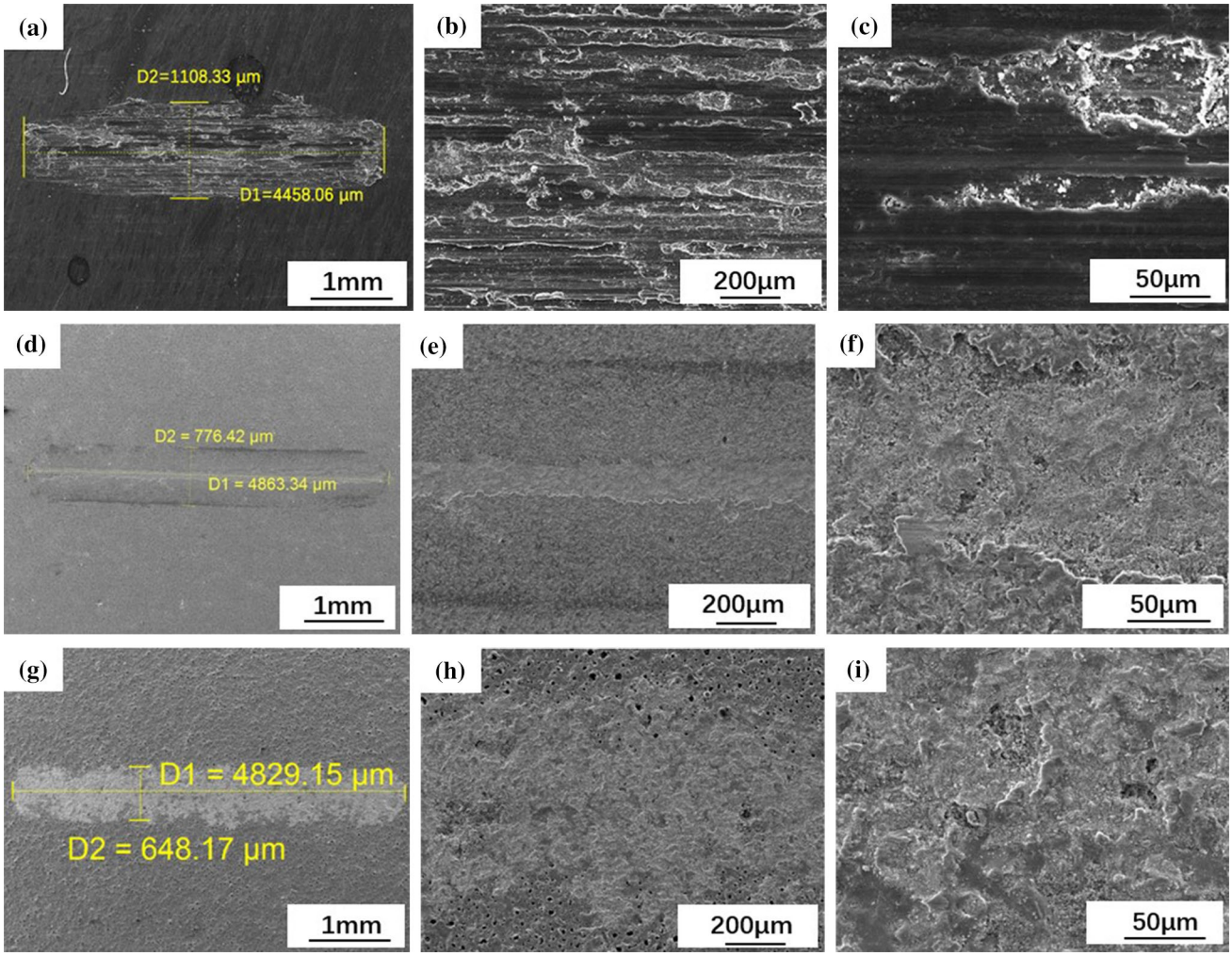

Fig. 15 SEM images showing the wear track morphologies of uncoated D16T, G0 and G2: (a-c) uncoated D16T; (d-f) G0 and (g-i) G2

Table 3 Component content of the wear tracks of uncoated D16T, G0 and G2

Element	C	O	Al	Fe	Cr
Uncoated D16T	…	12.435	81.185	…	…
G0	…	21.138	38.832	10.960	0.169
G2	14.127	23698	25.473	22.634	0.398

resistance is significantly improved. Liu et al. (Ref 40) clarified the mechanism that graphene nanosheets incorporated in the coating of aluminum alloy significantly improved the wear resistance by wear model and revealed that the graphene coating in form of embedded mode had higher adhesion than the graphene incorporated in the coating with spreading mode. From the above analysis, it can be seen that Al_2O_3 in the coating G2 increases and the crystallinity is improved. Its thickness and hardness increase, and the surface of the coating gets flatter and the number of micro-pores on the outer layer reduces. Furthermore, c-Al_2O_3 phase with high hardness improves the wear resistance of the coating. Parts of graphene entering the coating exist in the way of filling micro-pores and cracks, and part graphene exists in the way of spreading. The C atom from graphene with the strong van der Waals force does the relative movement under the external load (Ref 41). Therefore, during the process of continuous friction, graphene flatly adhered to the surface of the coating. Some graphene were compressed tighter and stronger under the load, which better filled the pores and cracks. The graphene and ceramic particles mixed each other and furtherly reduced the abrasive wear caused by the contact between the material and the steel ball. Graphene as a lubricant makes the composite coating own self-lubricating (Ref 6). With the increase in wear time, graphene gradually lost and the lubricity of the coating reduced, so the friction coefficient gradually increased and finally it reached that of G0.

4. Conclusion

(1) The coating is mainly composed of a-Al_2O_3 and c-Al_2O_3 phase. The crystalline character significantly increases, and the thickness of the coating with graphene increases slightly. The thickness of the dense layer increases from 0.6 to 1 **1**m. The surface of G2 is flat, and

very few molten particles, micro-pores and micro-cracks exist on the surface of the coating. Incorporated graphene in the coating fills the micro-pores and cracks and participated in the coating formation in the mode of A-type and C-type discharge and then agglomerates formed. The roughness of G2 is smaller than that of G0, and its hardness is significantly improved.

(2) The corrosion resistance of G2 coating is greatly improved due to the successful incorporation of graphene. The corrosion potential increased and corrosion current density decreased, and the polarization resistance increased to an order of magnitude. The corrosion rate reduced by nearly 8 times for G2 coating as compared to that of G0.

(3) The wear resistance of the substrate was greatly improved by MAO treatment technique. Adhesive wear transforms to abrasive wear for the coated samples. Incorporation of graphene had impact on pores and cracks in the coating and improved the compactness and hardness of the coating. During the abrasion process, the graphene on the surface of the coating fall off and some graphene entered to the micro-pores under the wear back and forth and strengthen the coating. That acts as a lubricant function among the friction pairs with a steady-state sheet structure. The friction coefficient of G2 reduces and its wear resistance is significantly improved compared to that of G0.

Acknowledgments

The authors wish to thank the funding of the award of fellowship from China Scholarship Council to Wanying Liu and the experiment equipment and technical guidance support by Helmholtz-Zentrum Geesthacht. Authors are thankful to the financial assistance provided by the National Natural Science Foundation of China (No. 52074232 and No. 51904261), the 19th and 20th college students' key open experimental subjects of Southwest Petroleum University (KSZ19503), Sichuan Youth Science and Technology Innovation Research Team Project Plan (2020JDTD0016).

References

1. C. Santus, L. Bertini, M. Beghini, A. Merlo and A. Baryshnikov, Torsional Strength Comparison Between Two Assembling Techniques for Aluminium Drill Pipe to Steel Tool Joint Connection, *Int. J. Pres. Ves. Pip.*, 2009, 86(2–3), p 177–186
2. W. Liu, Y. Liu, W. Chen, T. Shi, A. Singh and Q. Lu, Longitudinal Crack Failure Analysis of Box of S135 Tool Joint in Ultra-Deep Well, *Eng. Fail. Anal.*, 2015, 48, p 283–296
3. A.I. Shakirova, R.A. Ismakov and A.K. Agliullin, Comprehensive Studies of Aluminum Drill Pipe Materials, *Bull. Tomsk Polytech. Univ.-Geo Assets Eng.*, 2017, 328, p 95–103
4. R.A. Erin, Aluminum Alloy Drill Pipe in Geothermal Drilling, *Proceedings World Geothermal Congress 2010*, Bali, Indonesia, 2010, p 25–29
5. W. Liu, Y. Liu, Y. Lin, Z. Zhang, S. Feng, M. Talha, Y. Shi and T. Shi, Effects of Graphene on Structure and Corrosion Resistance of Plasma Electrolytic Oxidation Coatings Formed on D16T Al Alloy, *Appl. Surf. Sci.*, 2019, 475, p 645–659
6. L. Wen, Y. Wang, Y. Zhou, L. Guo and J. Ouyang, Microstructure and Corrosion Resistance of Modified 2024 Al Alloy Using Surface Mechanical Attrition Treatment Combined with Microarc Oxidation Process, *Corros. Sci.*, 2011, 53(1), p 473–480
7. M. Javidi and H. Fadaee, Plasma Electrolytic Oxidation of 2024–T3 Aluminum Alloy and Investigation on Microstructure and Wear Behavior, *Appl. Surf. Sci.*, 2013, 286, p 212–219
8. X. Chen, D. Liao, D. Zhang, X. Jiang, P. Zhao and R. Xu, Effect of Content of Graphene on Corrosion Behavior of Micro-arc Oxidation Coating on Titanium Alloy Drill Pipe, *Int. J. Electrochem. Sci.*, 2020, 15, p 710–721
9. P. Ahmadi, A.A. Sarabi, H. Eivaz Mohammadloo and R. Behgam, Effect of practical parameters on the structure and corrosion behavior of vanadium/zirconium conversion coating on AA 2024 aluminum alloy, *J. Coat. Technol. Res.*, 2019, 16(5), p 1503–1513
10. A. Bahramian, K. Raeissi and A. Hakimizad, An investigation of the Characteristics of Al_2O_3/TiO_2 PEO Nanocomposite Coating, *Appl. Surf. Sci.*, 2015, 351, p 13–26
11. K. Babaei, A. Fattah-alhosseini and M. Molaei, The Effects of Carbon-Based Additives on Corrosion and Wear Properties of Plasma Electrolytic Oxidation (PEO) Coatings Applied on Aluminum and Its Alloys: A Review, *Surf. Interface.*, 2020, 21, p 100677
12. S. Fatimah, M.P. Kamil and J.H. Kwon, Dual Incorporation of SiO_2 and ZrO_2 Nanoparticles into the Oxide Layer on 6061 Al Alloy Via Plasma Electrolytic Oxidation: Coating Structure and Corrosion Properties, *J. Alloys Compd.*, 2017, 707, p 358–364
13. S. Ma, X. Suo and J. Qiu, Fabrication of n-SiO_2 Reinforced Al_2O_3 Composite Coatings on 7A52 Aluminium Alloy by Micro-arc Oxidation, *Adv. Mater. Res.*, 2010, 97–101, p 1463–1466
14. Q. Chen, Z. Jiang, S. Tang, W. Dong, Q. Tong and W. Li, Influence of Graphene Particles on the Micro-arc Oxidation Behaviors of 6063 Aluminum Alloy and the Coating Properties, *Appl. Surf. Sci.*, 2017, 423, p 939–950
15. M.F. Maqsood, M.A. Raza, F.A. Ghauri, Z.U. Rehman and M.T. Ilyas, Corrosion Study of Graphene Oxide Coatings on AZ31B Magnesium Alloy, *J. Coat. Technol. Res.*, 2020, 17(5), p 1321–1329
16. W. Liu, C. Blawert, M.L. Zheludkevich, Y. Lin, M. Talha, Y. Shi and L. Chen, Effects of Graphene Nanosheets on the Ceramic Coatings Formed on Ti6Al4V Alloy Drill Pipe by Plasma Electrolytic Oxidation, *J. Alloys Compd.*, 2019, 789, p 996–1007
17. A. Khakzad, S.M. Mousavi Khoi, S.A. Tayebifard, E. Aghaie, Y. Behnamian, M. Mozammel and H. Maleki-Ghaleh, Alumina-Silica Composite Coatings on Aluminum by Plasma Electrolytic Oxidation: The Effect of Coating TIME on Microstructure, Phase, and Corrosion Behavior, *J. Mater. Eng. Perform.*, 2017, 26(6), p 2663–2670
18. K.J. Ma, M.M.S. Bosta and W.T. Wu, Preparation of Self-lubricating Composite Coatings through a Micro-arc Plasma Oxidation with Graphite in Electrolyte Solution, *Surf. Coat. Tech.*, 2014, 259, p 318–324
19. G.H. Lv, H. Chen, W.C. Gu, W.R. Feng, L. Li, E.W. Niu, X.H. Zhang and S.Z. Yang, Effects of Graphite Additives in Electrolytes on the Microstructure and Corrosion Resistance of Alumina PEO Coatings, *Curr. Appl. Phys.*, 2009, 9(2), p 324–328
20. Y. Guan, Y. Xia and G. Lia, Growth Mechanism and Corrosion Behavior of Ceramic Coatings on Aluminum Produced by Autocontrol AC Pulse PEO, *Surf. Coat. Tech.*, 2008, 202(19), p 4602–4612
21. G. Yang, X. Lu, Y. Bai, H. Cui and Z. Jin, The Effects of Current Density on the Phase Composition and Microstructure Properties of Micro-arc Oxidation Coating, *J. Alloys Compd.*, 2002, 345(1–2), p 196–200
22. Z.J. Wang, L.N. Wu, W. Cai, A. Shan and Z.H. Jiang, Effects of Fluoride on the Structure and Properties of Microarc Oxidation Coating on Aluminium Alloy, *J. Alloys Compd.*, 2010, 505(1), p 188–193
23. M. Kaseem, M.P. Kamil and Y.G. Ko, Electrochemical Response of MoO_2-Al_2O_3 Oxide Films Via Plasma Electrolytic Oxidation, *Surf. Coat. Tech.*, 2017, 322, p 163–173
24. N.P. Wasekar, A. Jyothirmayi, L.R. Krishna and G. Sundararajan, Effect of Micro Arc Oxidation Coatings on Corrosion Resistance of 6061-Al Alloy, *J. Mater. Eng. Perform.*, 2009, 17(5), p 108–713
25. E. Matykina, R. Arrabal, F. Monfort, P. Skeldon and G.E. Thompson, Incorporation of Zirconia into Coatings Formed by DC Plasma Electrolytic Oxidation of Aluminum in Nanoparticles Suspensions, *Appl. Surf. Sci.*, 2008, 255(5), p 2830–2839
26. M. Tang, Z. Feng, G. Li, Z. Zhang and R. Zhang, High-Corrosion Resistance of the Microarc Oxidation Coatings on Magnesium Alloy

Obtained in Potassium Fluotitanate Electrolytes, *Surf. Coat. Tech.*, 2015, 264, p 105–113
27. D. Salehi Doolabi, M. Ehteshamzadeh and S.M.M. Mirhosseini, Effect of NaOH on the Structure and Corrosion Performance of Alumina and Silica PEO Coatings on Aluminum, *J. Mater. Eng. Perform.*, 2012, 21(10), p 2195–2202
28. M. Laleh, R.T. Sabour and A. Shanghi, Effect of Alumina Sol Addition to Micro-arc Oxidation Electrolyte on the Properties of MAO Coatings Formed on Magnesium Alloy AZ91D, *J. Alloys Compd.*, 2010, 496(1–2), p 548–552
29. R.O. Hussein, X. Nie, D.O. Northwood, A. Yerokhin and A. Matthews, Spectroscopic Study of Electrolytic Plasma and Discharging Behaviour During the Plasma Electrolytic Oxidation (PEO) Process, *J. Phys. D: Appl. Phys.*, 2010, 43(10), p 185–203
30. Y. Cheng, Z. Xue, Q. Wang, X. Wu, E. Matykina, P. Skeldon and G.E. Thompson, New Findings on Properties of Plasma Electrolytic Oxidation Coatings from Study of an Al-Cu-Li Alloy, *Electrochim. Acta*, 2013, 107, p 358–378
31. C.L. Yeh and C.W. Kuo, Effects of Al and Al_4C_3 Contents on Combustion Synthesis of Cr_2AlC from Cr_2O_3-Al-Al_4C_3 Powder Compacts, *J. Alloys Compd.*, 2011, 509(3), p 651–655
32. G. Jang, M. Slesar and M. Besterci, Mechanismus der dispersionshärtung von aluminium mit Al_4C_3, *Z. Werkstofftech.*, 1987, 18, p 36–42
33. S.J. Richard Prabakar, Y.H. Hwang and E.G. Bae, SnO_2/Graphene Composites with Self-assembled Alternating Oxide and Amine Layers for high Li-Storage and Excellent Stability, *Adv. Mater.*, 2013, 25(24), p 3307–3312
34. H. Fadaee and M. Javidi, Investigation on the Corrosion Behaviour and Microstructure of 2024–T3 Al Alloy Treated Via Plasma Electrolytic Oxidation, *J. Alloys Compd.*, 2014, 604, p 36–42
35. M. Shokouhfar, C. Dehghanian, M. Montazeri and A. Baradaran, Preparation of Ceramic Coating on Ti Substrate by Plasma Electrolytic Oxidation in Different Electrolytes and Evaluation of Its Corrosion Resistance: Part II, *Appl. Surf. Sci.*, 2012, 258(7), p 2416–2423
36. P. Garg, P. Gupta, D. Kumar and O. Parkash, Structural and Mechanical Properties of Graphene Reinforced Aluminum Matrix Composites, *J. Mater. Environ. Sci.*, 2016, 7(5), p 1461–1473
37. J. Zhao, X. Xie and C. Zhang, Effect of the Graphene Oxide Additive on the Corrosion Resistance of the Plasma Electrolytic Oxidation Coating of the AZ31 Magnesium Alloy, *Corros. Sci.*, 2017, 114, p 146–155
38. W.D. Ling, P. Wei, J.Z. Duan, J.M. Chen and W.S. Duan, First-Principles Study of the Friction and Wear Resistance of Graphene Sheets, *Tribol. Lett.*, 2017, 65, p 53–61
39. Y. Ma, H.H. Di, Z.X. Yu, L. Liang, L. Lv, Y. Pan, Y.Y. Zhang and D. Yin, Fabrication of Silica-Decorated Graphene Oxide Nanohybrids and the Properties of Composite Epoxy Coatings Research, *Appl. Surf. Sci.*, 2016, 360(Part B), p 936–945
40. W.Y. Liu, Y. Liu, C. Blawert, M.L. Zheludkevich, C.L. Fan, M. Talha and Y.H. Lin, Microstructure, Wear and Corrosion Performance of Plasma Electrolytic Oxidation Coatings Formed on D16T Al Alloy, *Rare Met.*, 2020, 12(39), p 1425–1439
41. M. Qian, M.S. Andrew, X.H. Tan, X.T. Zeng and W.L. Sudesh, Two-Part Epoxy-Siloxane Hybrid Corrosion Protection Coatings for Carbon Steel, *Thin Solid Films*, 2009, 517(17), p 5237–5242